npj | 2D materials and applications

www.nature.com/npj2dmaterials

ARTICLE OPEN

Check for updates

Exploration of two-dimensional molybdenum-borides and potential applications

Junjie Jin[1] and Udo Schwingenschlögl[1]✉

The recent discovery of MBenes has generated interest in two-dimensional metal-borides, which are expected to show rich electrochemical properties. Using evolutionary search combined with ab initio calculations, we discover that the MoB_x ($x = 1$, 3, and 4) monolayers, two-dimensional metal-borides, are dynamically, mechanically, and thermally stable. Due to their metallic characters, we investigate the potential of application as anode materials of Li-ion batteries. The MoB and MoB_3 monolayers are found to provide excellent properties, combining high Li-specific capacities of 670 and 418 mA h g^{-1} with low Li diffusion barriers of 0.10 and 0.13 eV, respectively.

npj 2D Materials and Applications (2022)6:49 ; https://doi.org/10.1038/s41699-022-00319-3

INTRODUCTION

Rechargeable Li-ion batteries (LIBs), are widely used for energy storage in portable electronic devices and electric vehicles[1–6]. Improving the performance of the electrode materials is key for enhancing the energy density and extending the endurance. As compared to the rapid development of the cathode materials, the anode materials are still limited in their performance, particularly in their Li capacity[7]. Two-dimensional materials are promising options for battery anodes, enabling high energy density and ion mobility[8,9], and therefore are the subject of tremendous research efforts[10–13]. Recently, a class of two-dimensional metal-borides (MBenes) became experimentally accessible[14]. Theoretical analyses point at excellent electrochemical, catalytic, thermoelectric, and optical properties[15–17]. For example, the Fe_2B_2 monolayer exhibits an almost ideal Gibbs free energy for hydrogen evolution and a specific capacity of 665 mA h g^{-1} for LIBs[18]. The specific capacities of the Mo_2B_2 and Ti_2B_2 monolayers for LIBs are 444 and 558 mA h g^{-1}, respectively[18,19].

Considering that boron forms with metals a multitude of compounds with different stoichiometries[20], we were wondering whether there exit two-dimensional metal-borides that are suitable for application in LIBs. To answer this question, we execute in the present work an ab initio evolutionary search for new monolayer structures of metal-borides. In contrast to refs. [14,17], we aim for two-dimensional materials without dangling bonds saturated by termination groups. Such materials may be synthesized by a bottom-up approach (chemical vapor deposition or epitaxial growth, similar to borophene[21] and a variety of transition metal dichalcogenides[22]) rather than by a top-down approach. We discover the MoB_x ($x = 1$, 3, and 4) monolayers, which turn out to be metallic as required for fast electron transport and battery charging. The MoB and MoB_3 monolayers emerge as promising candidates for the anode of LIBs, combining the advantages of multilayer ion intercalation with high specific capacity, fast ion diffusion, and suitable open-circuit voltage.

RESULTS AND DISCUSSION

Our comprehensive structure search reveals four monolayers that have very low formation energy, see Fig. 1b, and thus are expected to be accessible experimentally. Their relaxed structures are shown in Fig. 1a. A summary of the structural information of the MoB_x ($x = 1$, 2, 3, and 4) monolayers is given in Table 1. The formation energy of the MoB monolayer (space group *P*–1) turns out to be 0.22 eV per atom lower than that of the recently reported tetragonal Mo_2B_2 monolayer[23]. We find optimized lattice parameters of $a = b = 3.10$ Å, a total thickness of 4.74 Å, and Mo-B bond lengths in the range of 2.09–2.37 Å. The tetragonal sandwich structure resembles that of the Ti_3C_3 monolayer[24]. The MoB_2 monolayer (space group *C*2/*m*) is dynamically instable, compare Fig. 2a. Complementary structure searches with fixed composition and maxima of 3, 6, 9, and 15 atoms in the unit cell do not result in an alternative structure with lower formation energy. Therefore, the MoB_2 monolayer is of no further interest. The MoB_3 monolayer (space group *Pmmm*) consists of a network of three-membered B rings with B-B bond lengths of 1.66 and 1.71 Å. The Mo atoms connect these rings with Mo–B bond lengths of 2.24 and 2.38 Å. We obtain optimized lattice parameters of $a = 4.64$ Å and $b = 2.97$ Å, and a total thickness of 3.01 Å. Finally, the MoB_4 monolayer (space group *C*2/*m*) features a hexagonal structure with optimized lattice parameters of $a = b = 2.97$ Å and a total thickness of 3.29 Å. We obtain for the cohesive energy $E_{coh} = (E_{Mo} + xE_B - E_{MoBx})/(x + 1)$, where E_{Mo}, E_B, and E_{MoBx} are the total energies of Mo, B, and the MoB_x monolayer, respectively, values of 6.37, 6.38, and 6.33 eV per atom for the MoB, MoB_3, and MoB_4 monolayers, which are close to that of the TiB_3 monolayer (6.35 eV per atom)[25] but higher than that of the Cr_2B_2 monolayer (5.87 eV per atom)[26].

The absence of negative phonon frequencies in Fig. 2a demonstrates dynamic stability of the MoB_x ($x = 1$, 3, and 4) monolayers. Notably, the highest phonon frequencies of the MoB (740 cm^{-1}), MoB_3 (1091 cm^{-1}), and MoB_4 (904 cm^{-1}) monolayers exceed those of experimentally demonstrated materials such as germanene (286 cm^{-1})[27], black phosphorene (470 cm^{-1})[28], MoS_2 (491 cm^{-1})[29], and silicene (554 cm^{-1})[28]. Our AIMD simulations, see

[1]Physical Science and Engineering Division (PSE), King Abdullah University of Science and Technology (KAUST), Thuwal 23955-6900, Saudi Arabia.
✉email: udo.schwingenschlogl@kaust.edu.sa

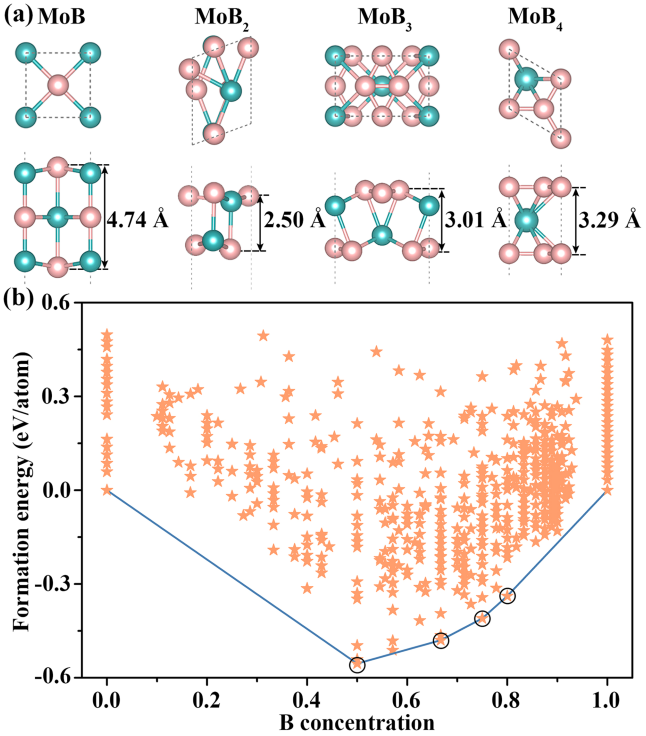

Fig. 1 Structure. a Top and side views of the MoB_x ($x = 1$, 2, 3, and 4) monolayers (pink balls = B atoms, blue balls = Mo atoms). **b** Formation energy per atom of MoB_x as a function of the B concentration $x/(x+1)$. The black circles mark the MoB_x ($x = 1$, 2, 3, and 4) monolayers.

Fig. 2b–d, exhibit no signs of structural disruption at 300 and 1000 K. The calculated elastic constants of the MoB_x ($x = 1$, 3, and 4) monolayers, listed in Table 2, show that the mechanical stability criteria $C_{11}C_{22}-{C_{12}}^2 > 0$ and $C_{66} > 0$ are satisfied in each case. We derive the direction dependences (θ = angle with respect to the x-axis) of Young's modulus

$$E(\theta) = \frac{C_{11}C_{22} - C_{12}^2}{C_{11}\sin^4\theta + [(C_{11}C_{22} - C_{12}^2)/C_{66} - 2C_{12}]\sin^2\theta\cos^2\theta + C_{22}\cos^4\theta}, \quad (1)$$

which characterizes the stiffness of a material, and Poisson's ratio

$$v(\theta) = \frac{C_{12}\sin^4\theta - [C_{11} + C_{22} - (C_{11}C_{22} - C_{12}^2)/C_{66}]\sin^2\theta\cos^2\theta + C_{12}\cos^4\theta}{C_{11}\sin^4\theta + [(C_{11}C_{22} - C_{12}^2)/C_{66} - 2C_{12}]\sin^2\theta\cos^2\theta + C_{22}\cos^4\theta}, \quad (2)$$

which characterizes the response of a material to external load, from the elastic constants. According to Fig. 3a, Young's modulus of the MoB monolayer is 297 N m^{-1} at $\theta = 0°$ and $\theta = 90°$, reaching at $\theta = 45°$ a maximum of 478 N m^{-1} in excess of that of graphene (334 N m^{-1})[24]. Young's modulus of the MoB_3 monolayer is 160 N m^{-1} at $\theta = 0°$ and 301 N m^{-1} at $\theta = 90°$ with a maximum of 370 N m^{-1} at $\theta = 57°$. Finally, Young's modulus of the MoB_4 monolayer is 387 N m^{-1} independent of θ. According to Fig. 3b, Poisson' ratio varies between 0.10 and 0.44 for the MoB monolayer, varies between 0.03 and 0.59 for the MoB_3 monolayer, and amounts to 0.16 for the MoB_4 monolayer. The electronic band structures in Fig. 3c–e show several bands crossing the Fermi energy, indicating excellent metallic behavior of the MoB_x ($x = 1$, 3, and 4) monolayers.

We use 2 × 2 × 1 supercells to determine the energetically favorable adsorption sites of Li on the MoB_x ($x = 1$, 3, and 4)

Table 1. Structural information of the MoB_x ($x = 1$, 2, 3, and 4) monolayers.

	Lattice parameters	Space group	Atom	Wyckoff position	x	y	z
MoB	$a = b = 3.10$ Å	P–1	B1	2i	0.53686	0.41030	0.49017
			B2	2i	0.03568	0.90982	0.39531
			B3	2i	0.54455	0.40934	0.30047
			Mo1	2i	0.53573	0.40983	0.39533
			Mo2	2i	0.03665	0.91022	0.47903
			Mo3	2i	0.03469	0.90940	0.31162
MoB_2	$a = 4.64$ Å, $b = 2.97$ Å	$C2/m$	B1	8j	0.07076	0.62245	0.44162
			B2	8j	0.37164	0.03656	0.56812
			B3	8j	0.64909	0.46459	0.43297
			B4	8j	0.95003	0.87861	0.55971
			Mo1	8j	0.36130	0.04289	0.45398
			Mo2	8j	0.65942	0.45829	0.54711
MoB_3	$a = 3.02$ Å, $b = 4.23$ Å	$Pmmm$	B1	8a	0.08844	0.38825	0.35418
			B2	8a	0.26741	0.88827	0.34829
			B3	8a	0.90937	0.88826	0.34830
			B4	8a	0.40955	0.38843	0.47363
			B5	8a	0.58860	0.88844	0.46773
			B6	8a	0.76760	0.38842	0.47366
			Mo1	8a	0.08854	0.88835	0.44140
			Mo2	8a	0.58839	0.38834	0.38053
MoB_4	$a = b = 2.97$ Å	$C2/m$	B1	8j	0.94153	0.48602	0.46369
			B2	8j	0.94123	0.48576	0.33216
			B3	8j	0.27458	0.15244	0.33218
			B4	8j	0.27488	0.15269	0.46371
			Mo1	8j	0.60804	0.81922	0.39795

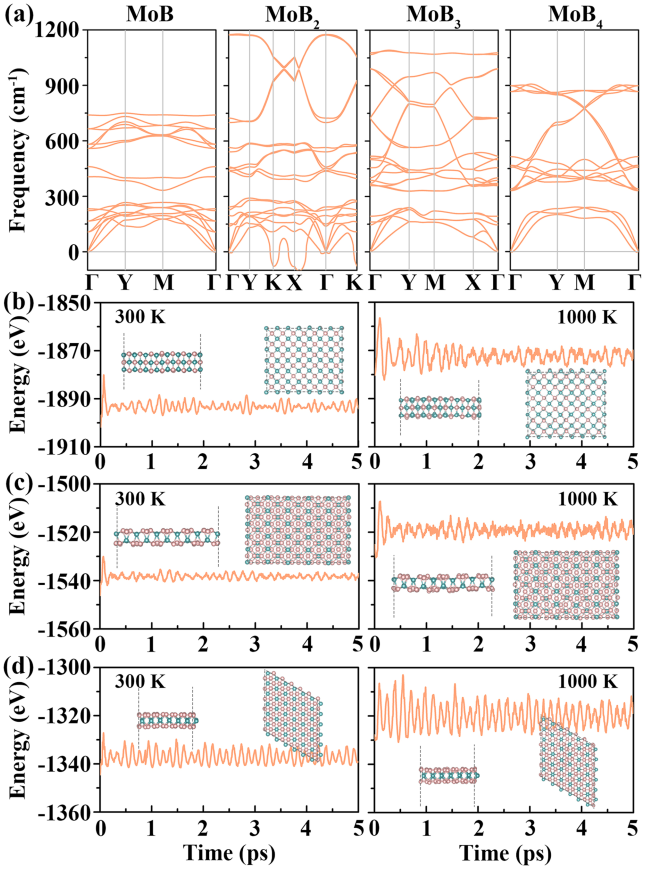

Fig. 2 Stability. a Phonon spectra of the MoB_x (x = 1, 2, 3, and 4) monolayers. Total energies during the AIMD simulations of the **b** MoB, **c** MoB_3, and **d** MoB_4 monolayers at 300 and 1000 K with top and side views of the final structures.

Table 2. In-plane elastic constants (N m^{-1}), Young's modulus (N m^{-1}), and Poisson's ratio.

Monolayer	C_{11}	C_{22}	C_{12}	C_{66}	$E(\theta = 0°)$	$E(\theta = 90°)$	$v(\theta = 0°)$	$v(\theta = 90°)$
MoB	369	369	163	217	297	297	0.44	0.44
MoB_3	191	365	110	160	160	301	0.30	0.59
MoB_4	397	397	62	168	387	387	0.16	0.16

monolayers, considering the sites marked in Fig. 4a. The adsorption energy is given by $E_{ad} = E_{MoBx+Li} - E_{MoBx} - E_{Li}$, where $E_{MoBx+Li}$ is the total energy when one Li atom is absorbed on the MoB_x monolayer. Any anode material for LIBs must spontaneously adsorb Li, implying that E_{ad} must be negative. According to results in Fig. 4a, stable adsorption on the MoB monolayer is possible on top of the center of the Mo_2B_2 ring (S1), on the top of B (S2), and on top of Mo (S3). Stable adsorption on the MoB_3 monolayer is possible on top of the center of the Mo_2B_2 ring (S1), on top of the B–B bond (S2), on top of Mo (S3), and on top of the center of the Mo_2B_4 ring (S4), whereas a Li atom adsorbed on top of B (S5) shifts to the S2 site during the structure optimization. Stable adsorption on the MoB_4 monolayer is possible on top of Mo (S1), whereas a Li atom adsorbed on top of B (S2) shifts to the S1 site during structure optimization. In each case, the S1 site turns out to be energetically favorable for Li adsorption. The obtained values of E_{ad} and corresponding adsorption heights are reported in Table 3. Furthermore, the charge redistributions between Li and

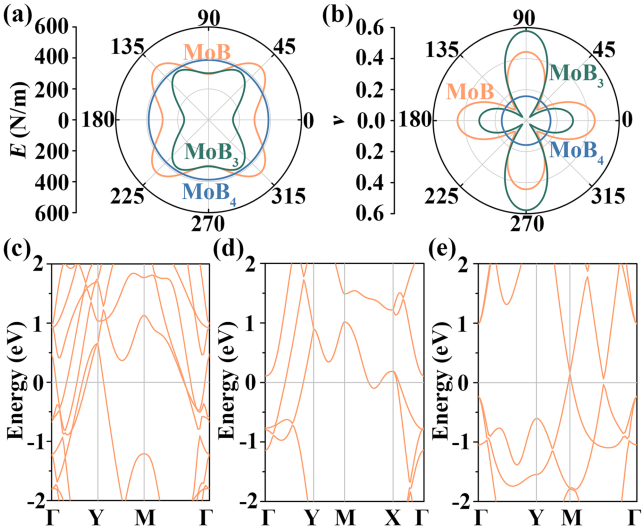

Fig. 3 Structural and electronic properties. a Young's moduli, **b** Poisson's ratios, and **c**–**e** electronic band structures of the MoB_x (x = 1, 3, and 4) monolayers.

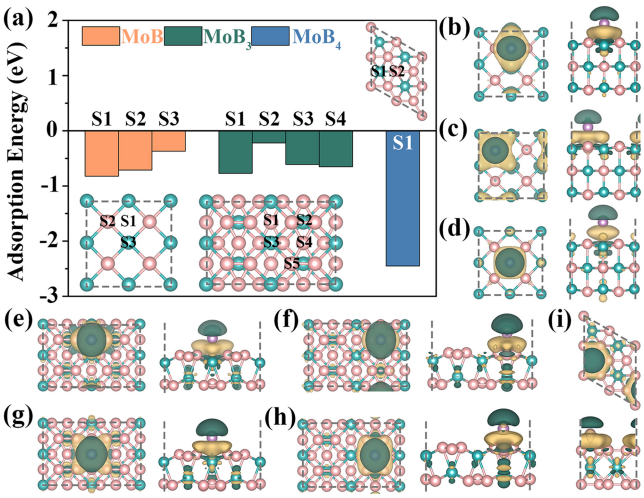

Fig. 4 Li adsorption. a Adsorption energies of Li on the MoB_x (x = 1, 3, and 4) monolayers. The insets show the considered adsorption sites. Top and side views of the charge redistributions induced by the interaction of Li at the **b** S1, **c** S2, and **d** S3 sites with the MoB monolayer, by the interaction of Li at the **e** S1, **f** S2, **g** S3, and **h** S4 sites with the MoB_3 monolayer, and by the interaction of Li at the **i** S1 site with the MoB_4 monolayer. Green and yellow isosurfaces (isovalue: 0.01 electrons/Å^3) represent charge depletion and accumulation, respectively.

the MoB_x (x = 1, 3, and 4) monolayers are presented in Fig. 4b–i for the different adsorption sites, showing that Li acts as a charge donor. Bader charge analysis results in charge transfers of 0.85–0.88 electrons, see Table 3.

The Li-specific capacity is a key performance indicator of a LIB. To determine its value, we employ 2 × 2 × 1 supercells of the MoB_x (x = 1, 3, and 4) monolayers and consider potential multilayer adsorption on both sides of the monolayers. The average Li adsorption energy of the nth Li layer is given by $E_{ave} = (E_{MoBx+nLi} - E_{MoBx+(n-1)Li} - \lambda E_{Li})/\lambda$, where $E_{MoBx+nLi}$ and $E_{MoBx+(n-1)Li}$ are the total energies of the MoB_x monolayer with n and n–1 layers of adsorbed Li atoms, respectively, and λ is the number of atoms in the nth Li layer. In the case of the MoB

monolayer we obtain $E_{ave} = -0.42$, -0.36, and -0.01 eV for the first (located at the S1 sites, see Fig. 5a), second (located at the S3 sites, see Fig. 5b), and third (located at the S2 sites, see Fig. 5c) Li layer, respectively. In the case of the MoB_3 monolayer the atoms in the first Li layer are located at the S1 and S4 sites (see Fig. 5d) and we obtain $E_{ave} = -0.73$ eV. However, already for the first Li atom in the second layer the adsorption energy is positive for all possible adsorption sites, i.e., it is not adsorbed but Li dendrite growth is to be expected. Similarly, in the case of the MoB_4 monolayer only one Li layer is formed (located at the S1 sites, see Fig. 5e) and we find $E_{ave} = -1.55$ eV. Overall, the $2 \times 2 \times 1$ supercells of the MoB_x ($x = 1$, 3, and 4) monolayers can accommodate $x_{max} = 32$, 16, and 8 Li atoms, respectively. Figure 5f–h shows the formation energy of MoB_xLi_m relative to the MoB_x monolayer and bulk Li. Location of $MoBLi_{2.67}$, MoB_3Li_2, and MoB_4Li_2 on the convex hull demonstrates stability at full Li loading. The Li specific capacity is given by $C = x_{max}F/M$, where F is the Faraday constant (26801 mA h mol^{-1}) and M is the relative molecular mass of the MoB_x monolayer. We obtain $C = 670$ mA h g^{-1} for $MoBLi_{2.67}$, $C = 418$ mA h g^{-1} for MoB_3Li_2, and $C = 385$ mA h g^{-1} for MoB_4Li_2 in excess of the Li-specific capacity of graphite (372 mA h g^{-1})[30]. The MoB monolayer additionally outperforms the potential 2D anode materials Ti_2NS_2 (308 mA h g^{-1})[31], $Ti_3C_2S_2$ (463 mA h g^{-1})[32], Mo_2C (526 mA h g^{-1})[33], and V_3C_2 (606 mA h g^{-1})[34]. We also find that the lattice constants of the MoB_x ($x = 1$, 3, and 4) monolayers increase at most by 2.1, 1.7, and 1.0% during the lithiation process, respectively, and that the metallicity is maintained, see Fig. 5, which is a prerequisite of the anode operation.

Table 3. Adsorption energies (eV), adsorption heights (Å), and charge transfers (electrons) of Li on the MoB_x ($x = 1$, 3, and 4) monolayers.

Monolayer	Site	E_{ad}	h	Δq
MoB	S1	−0.82	2.15	0.85
	S2	−0.71	2.16	0.85
	S3	−0.37	2.40	0.86
MoB_3	S1	−0.77	1.71	0.86
	S2	−0.22	1.98	0.88
	S3	−0.61	1.72	0.88
	S4	−0.65	1.74	0.87
	S5	Converges to the S2 site		
MoB_4	S1	−2.45	1.56	0.85
	S2	Converges to the S1 site		

We next study the open-circuit voltage as another important performance indicator of a LIB, given by $V_{OCV} \sim (E_{MoBx} + zE_{Li} - E_{MoBx+zLi})/ze$, where $E_{MoBx+zLi}$ is the total energy when z Li atoms are absorbed on the MoB_x monolayer. We observe a decrease from 0.88 V at $z = 8$ to 0.31 V at $z = 32$ for the MoB monolayer, a decrease from 0.77 V at $z = 1$ to 0.73 V at $z = 16$ for the MoB_3 monolayer (<1 V, implying that Li dendrite growth can be avoided), and a decrease from 2.45 V at $z = 1$ to 1.55 V at $z = 8$ for the MoB_4 monolayer (pointing to Li dendrite growth, i.e., the MoB_4 monolayer is of no further interest in the following). The electron localization functions given in Fig. 6 show for the MoB monolayer that electrons are shifted towards to surface, which stabilizes the Li adsorption by reducing the repulsion. Specifically, Bader charge analysis indicates that each atom in the outer Li layer obtains 0.3 electrons from the inner Li layers. Finally, AIMD simulations of $MoBLi_{2.67}$ and MoB_3Li_2, see Fig. 7, exhibit no sign of structural disruption during battery operation at 300 K.

The Li diffusion determines the critical charging and discharging rates of the battery. Figure 8 presents the Li diffusion pathways on the MoB and MoB_3 monolayers. In the case of the MoB monolayer

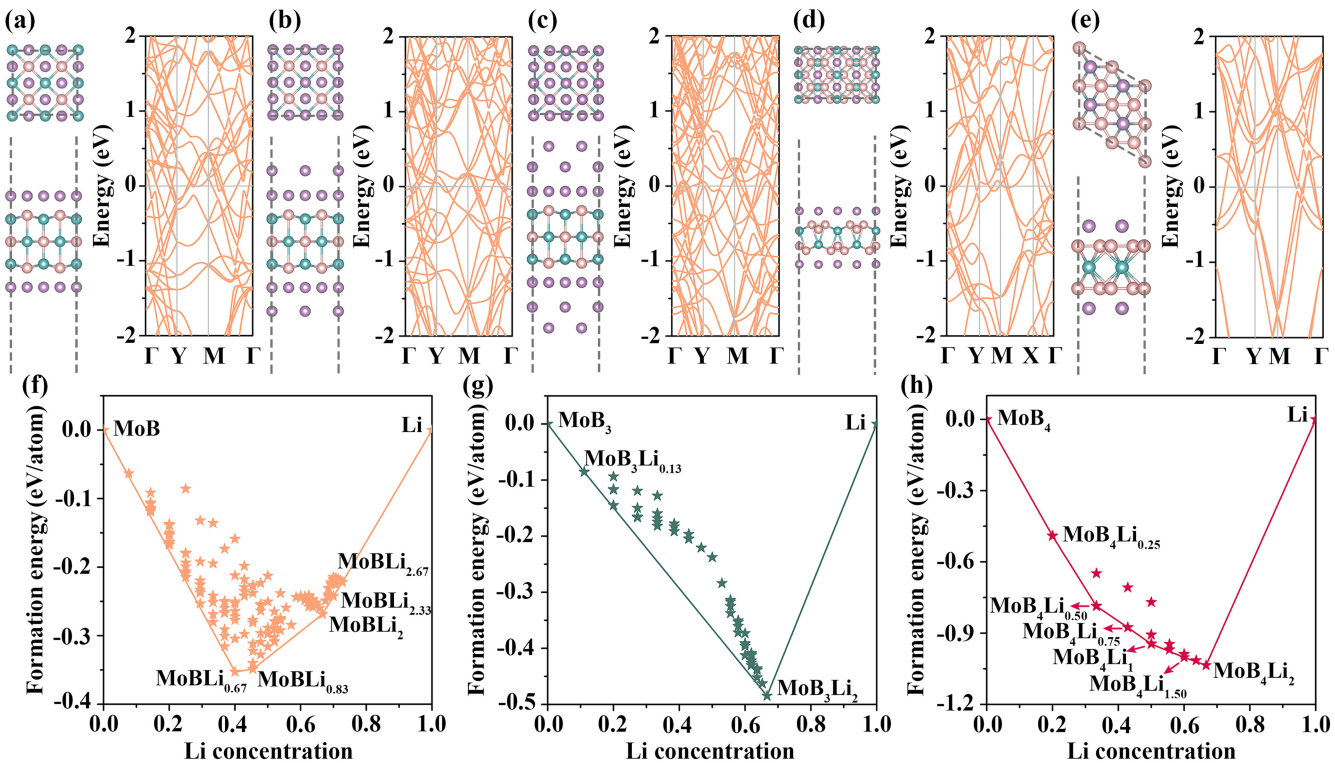

Fig. 5 Li adsorption. Top and side views as well as electronic band structures of the MoB monolayer with **a** one, **b** two, and **c** three layers of adsorbed Li atoms and **d** of the MoB_3 monolayer with one layer of adsorbed Li atoms, and **e** of the MoB_4 monolayer with one layer of adsorbed Li atoms. **f–h** Formation energy per atom of MoB_xLi_m ($x = 1$, 3, and 4) as function of the Li concentration $m/(m+1)$.

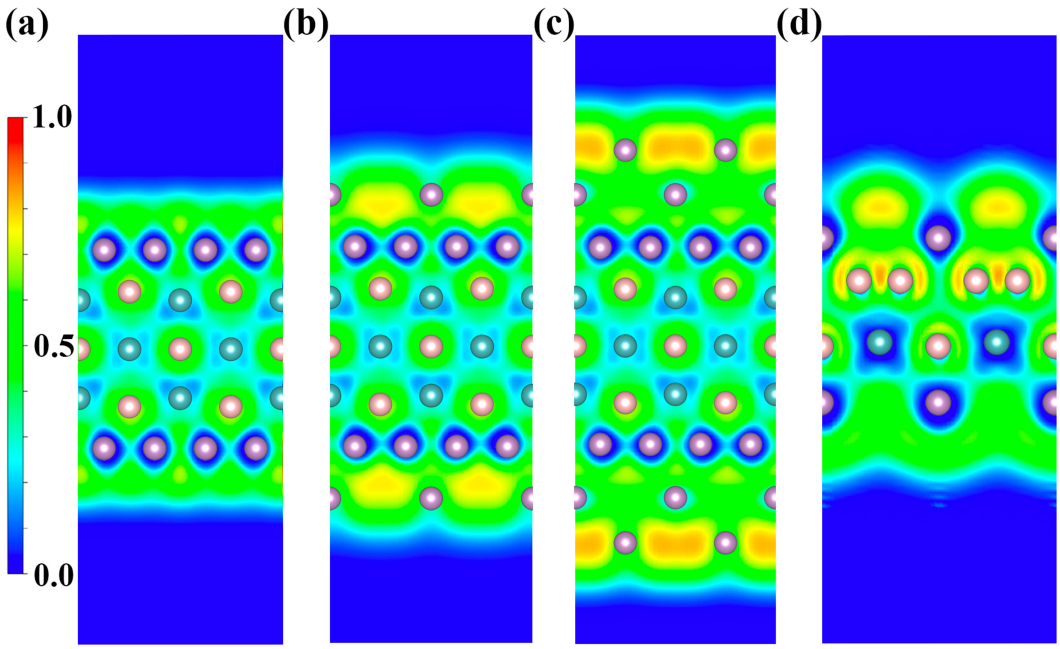

Fig. 6 Li adsorption. Electron localization functions of the MoB monolayer with **a** one, **b** two, and **c** three layers of adsorbed Li atoms [(110) plane], and **d** of the MoB_3 monolayer with one layer of adsorbed Li atoms [(010) plane].

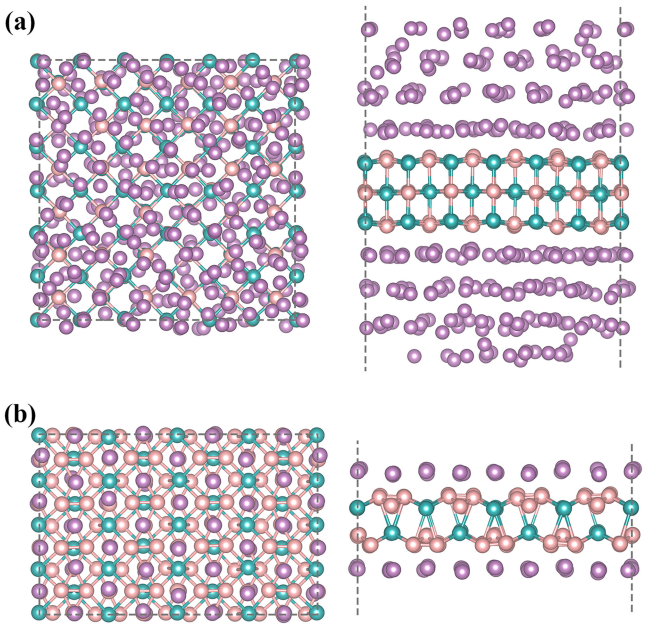

Fig. 7 Li adsorption. Top and side views of the **a** MoB and **b** MoB_3 monolayers with maximal Li adsorption after the AIMD simulations at 300 K.

there are three diffusion pathways between neighboring S1 sites. We obtain for path 1 (S1 → S2 → S1) a diffusion length of 3.14 Å and a diffusion barrier of 0.11 eV, for path 2 (S1 → S1) a diffusion length of 2.37 Å and a diffusion barrier of 0.10 eV, and for path 3 (S1 → S3 → S1) a diffusion length of 3.41 Å and a diffusion barrier of 0.45 eV. In the case of the MoB_3 monolayer there are only two diffusion pathways between neighboring S1 sites. For path 1 (S1 → S3 → S1) the diffusion length is 2.93 Å and the diffusion barrier is 0.16 eV, while for path 2 (S1 → S4 → S1) the diffusion length is 5.49 Å and the diffusion barrier is 0.13 eV. Therefore, path 2 is energetically favorable for both the MoB and MoB_3 monolayers. Importantly, the obtained Li diffusion barriers are significantly lower than those reported for the potential 2D anode materials Ti_2CS_2 (0.22 eV)[35], silicene (0.24 eV)[36], and Cr_2B_2 (0.28 eV)[26], and much lower than that of graphite as the commercial anode material of LIBs (0.48 eV)[37]. A low Li diffusion barrier ensures high Li mobility and, consequently, high charging and discharging rates.

Ab initio evolutionary search points to the existence of three 2D molybdenum-borides that are highly stable according to the calculated phonon spectra, cohesive energies, and elastic constants as well as the results of AIMD simulations at room and elevated temperatures. Systematic investigation of the application potential of the monolayers as anode materials for LIBs shows that the MoB_4 monolayer is not suitable. On the other hand, the properties obtained for the MoB and MoB_3 monolayers are very promising. In particular, the high Li specific capacity (670 mA h g^{-1}) and low Li diffusion barrier (0.10 eV) of the MoB monolayer clearly surpass the key performance indicators of graphite.

METHODS

We employ the USPEX[38–40] code to perform a global structure search for different Mo:B ratios and a maximum of 16 atoms in the primitive unit cell. The population size is set to 100 and the number of generations is set to 50. We adopt density functional theory (Vienna Ab-initio Simulation Package[41]) to perform structural relaxations (in which the atomic positions, unit cell volume, and unit cell shape are considered as free parameters) and electronic structure calculations with the exchange-correlation functionals of Perdew–Burke–Ernzerhof and Heyd–Scuseria–Ernzerhof, respectively. A semi-empirical correction is used to account for the van der Waals interaction[42]. The plane wave cutoff energy is set to 500 eV, and the total energy and atomic forces are converged to 10^{-6} eV and 0.01 eV/Å, respectively. A Monkhorst–Pack k-sampling with 0.015 $Å^{-1}$ spacing is used. Addition of a 20 Å thick vacuum slab to each simulation cell ensures two-dimensional geometries. The PHONOPY code is used to calculate the phonon band structures[43]. Ab initio molecular dynamics (AIMD) simulations are carried out using a canonical ensemble and a Nosé–Hoover temperature

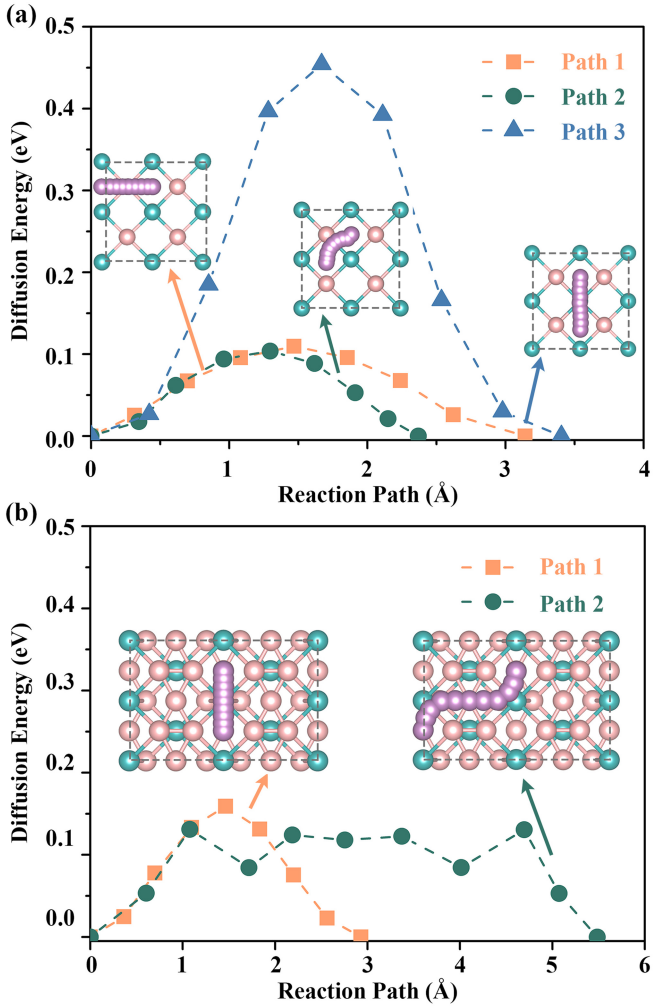

Fig. 8 Li adsorption. Li diffusion barriers on the **a** MoB and **b** MoB_3 monolayers for the diffusion pathways shown as insets.

control[44]. They are conducted at 300 and 1000 K for 5 ps with a time step of 1 fs for 6 × 6 × 1, 5 × 5 × 1, and 6 × 6 × 1 supercells of the MoB, MoB_3, and MoB_4 monolayers, respectively. The Li diffusion barrier and pathway are derived by the climbing-image nudged elastic band method[45].

DATA AVAILABILITY

The data supporting the findings of this study are available within the article.

CODE AVAILABILITY

No custom code is used.

Received: 4 November 2021; Accepted: 10 June 2022;
Published online: 18 July 2022

REFERENCES

1. Dunn, B., Kamath, H. & Tarascon, J.-M. Electrical energy storage for the grid: A battery of choices. *Science* **334**, 928–935 (2011).
2. Zubi, G., Dufo-López, R., Carvalho, M. & Pasaoglu, G. The lithium-ion battery: State of the art and future perspectives. *Renew. Sust. Energ. Rev.* **89**, 292–308 (2018).
3. Cano, Z. P. et al. Batteries and fuel cells for emerging electric vehicle markets. *Nat. Energy* **3**, 279–289 (2018).
4. Li, M., Lu, J., Chen, Z. & Amine, K. 30 years of lithium-ion batteries. *Adv. Mater.* **30**, 1800561 (2018).
5. Liang, Y. et al. A review of rechargeable batteries for portable electronic devices. *InfoMat* **1**, 6–32 (2019).
6. Xie, J., Lu, Y. C. & Retrospective, A. on lithium-ion batteries. *Nat. Commun.* **11**, 2499 (2020).
7. Qian, J. et al. High rate and stable cycling of lithium metal anode. *Nat. Commun.* **6**, 63362 (2015).
8. Etacheri, V., Marom, R., Elazari, R., Salitra, G. & Aurbach, D. Challenges in the development of advanced Li-ion batteries: A review. *Energy Environ. Sci.* **4**, 3243–3262 (2011).
9. Xue, Y. et al. Opening two-dimensional materials for energy conversion and storage: A concept. *Adv. Energy Mater.* **7**, 1602684 (2017).
10. Oganov, A. R., Pickard, C. J., Zhu, Q. & Needs, R. J. Structure prediction drives materials discovery. *Nat. Rev. Mater.* **4**, 331–348 (2019).
11. Jana, S., Thomas, S., Lee, C. H., Jun, B. & Lee, S. U. B_3S monolayer: Prediction of a high-performance anode material for lithium-ion. *Batteries, J. Mater., Chem. A* **7**, 12706–12712 (2019).
12. Tang, C., Kour, G. & Du, A. Recent progress on the prediction of two-dimensional materials using CALYPSO. *Chin. Phy. B* **10**, 107306 (2019).
13. Zhu, C. et al. Ultrahigh capacity 2D anode materials for lithium/sodium-ion batteries: An entirely planar B_7P_2 monolayer with suitable pore size and distribution. *J. Mater. Chem. A* **8**, 10301–10309 (2020).
14. Zhou, J. et al. Boridene: Two-dimensional $Mo_{4/3}B_{2-x}$ with ordered metal vacancies obtained by chemical exfoliation. *Science* **373**, 801–805 (2021).
15. Zha, X. H., Xu, P., Huang, Q., Du, S. & Zhang, R.-Q. Mo_2B, An MBene member with high electrical and thermal conductivities, and satisfactory performances in lithium ion batteries. *Nanoscale Adv.* **2**, 347–355 (2020).
16. Guo, X. et al. Establishing a theoretical landscape for identifying basal plane active 2D metal borides (MBenes) toward nitrogen electroreduction. *Adv. Funct. Mater.* **31**, 2008056 (2021).
17. Helmer, P. et al. Investigation of 2D boridene from first principles and experiments. *Adv. Funct. Mater.* **32**, 2109060 (2022).
18. Guo, Z., Zhou, J. & Sun, Z. New two-dimensional transition metal borides for Li ion batteries and electrocatalysis. *J. Mater. Chem. A* **5**, 23530 (2017).
19. Bo, T. et al. Hexagonal Ti_2B_2 monolayer: A promising anode material offering high rate capability for Li-ion and Na-ion batteries. *Phys. Chem. Chem. Phys.* **20**, 22168–22178 (2018).
20. Akopov, G., Yeung, M. T. & Kaner, R. B. Rediscovering the crystal chemistry of borides. *Adv. Mater.* **29**, 1604506 (2017).
21. Li, G. et al. Epitaxial growth and physical properties of 2D materials beyond graphene: From monatomic materials to binary compounds. *Chem. Soc. Rev.* **47**, 6073–6100 (2018).
22. Cai, Z., Liu, B., Zou, X. & Cheng, H. Chemical vapor deposition growth and applications of two-dimensional materials and their heterostructures. *Chem. Rev.* **118**, 6091–6133 (2018).
23. Bo, T., Liu, P.-F., Zhang, J., Wang, F. & Wang, B.-T. Tetragonal and trigonal Mo_2B_2 monolayers: Two new low-dimensional materials for Li-ion and Na-ion batteries. *Phys. Chem. Chem. Phys.* **21**, 5178–5188 (2019).
24. Sun, M. & Schwingenschlögl, U. Structure prototype outperforming MXenes in stability and performance in metal-ion batteries: A high throughput study. *Adv. Energy Mater.* **11**, 2003633 (2021).
25. Li, R. et al. TiB_3 monolayer with a lower electrostatic-potential surface as a higher-performance anode material for Li-ion and Na-ion batteries. *Phys. Chem. Chem. Phys.* **22**, 22236–22243 (2020).
26. Jia, J., Li, B., Duan, S., Cui, Z. & Gao, H. Monolayer MBenes: Prediction of anode materials for high-performance lithium/sodium ion batteries. *Nanoscale* **11**, 20307–20314 (2019).
27. Peng, B. et al. Phonon transport properties of two-dimensional group-IV materials from ab initio calculations. *Phys. Rev. B* **94**, 245420 (2016).
28. Cai, Y. et al. Giant phononic anisotropy and unusual anharmonicity of phosphorene: Interlayer coupling and strain engineering. *Adv. Funct. Mater.* **25**, 2230–2236 (2015).
29. Cai, Y., Lan, J., Zhang, G. & Zhang, Y.-W. Lattice vibrational modes and phonon thermal conductivity of monolayer MoS_2. *Phys. Rev. B* **89**, 035438 (2014).
30. Winter, M., Besenhard, J. O., Spahr, M. E. & Novak, P. Insertion electrode materials for rechargeable lithium batteries. *Adv. Mater.* **10**, 725–763 (1998).
31. Shukla, V., Jena, N. K., Naqvi, S. R., Luo, W. & Ahuja, R. Modelling high-performing batteries with Mxenes: The case of S-functionalized two-dimensional nitride Mxene electrode. *Nano Energy* **58**, 877–885 (2019).
32. Yang, Z., Zheng, Y., Li, W. & Zhang, J. Tuning the electrochemical performance of Ti_3C_2 and Hf_3C_2 monolayer by functional groups for metal-ion battery applications. *Nanoscale* **13**, 11534–11543 (2021).

33. Sun, Q. et al. Ab initio prediction and characterization of Mo_2C monolayer as anodes for lithium-ion and sodium-ion batteries. *J. Phys. Chem. Lett.* **7**, 937–943 (2016).
34. Fan, K., Ying, Y., Li, X., Luo, X. & Huang, H. Theoretical investigation of V_3C_2 MXene as prospective high-capacity anode material for metal-ion (Li, Na, K, and Ca) batteries. *J. Phys. Chem. C* **123**, 18207–18214 (2019).
35. Wang, Y. et al. Achieving superior high-capacity batteries with the lightest Ti_2C MXene anode by first-principles calculations: Overarching role of S-functionate (Ti_2CS_2) and multivalent cations carrier. *J. Power Sources* **451**, 227791 (2020).
36. Zhuang, J. et al. Silicene: A promising anode for lithium-ion batteries. *Adv. Mater.* **29**, 1606716 (2017).
37. Toyoura, K., Koyama, Y., Kuwabara, A., Oba, F. & Tanaka, I. First-principles approach to chemical diffusion of lithium atoms in a graphite intercalation compound. *Phys. Rev. B* **78**, 214303 (2008).
38. Oganov, A. R. & Glass, C. W. Crystal structure prediction using ab initio evolutionary techniques: Principles and applications. *J. Chem. Phys.* **124**, 244704 (2006).
39. Oganov, A. R., Lyakhov, A. O. & Valle, M. How evolutionary crystal structure prediction works -and why. *Acc. Chem. Res.* **44**, 227–237 (2011).
40. Lyakhov, A. O., Oganov, A. R., Stokes, H. T. & Zhu, Q. New developments in evolutionary structure prediction algorithm USPEX. *Comput. Phys. Commun.* **184**, 1172–1182 (2013).
41. Kresse, G. & Joubert, D. From ultrasoft pseudopotentials to the projector augmented-wave method. *Phys. Rev. B* **59**, 1758–1775 (1999).
42. Grimme, S. Semiempirical GGA-type density functional constructed with a long-range dispersion correction. *J. Comput. Chem.* **27**, 1787–1799 (2006).
43. Togo, A. & Tanaka, I. First principles phonon calculations in materials science. *Scr. Mater.* **108**, 1–5 (2015).
44. Martyna, G. J., Klein, M. L. & Tuckerman, M. Nosé–Hoover chains: The canonical ensemble via continuous dynamics. *J. Chem. Phys.* **97**, 2635–2643 (1992).
45. Henkelman, G., Uberuaga, B. P. & Jónsson, H. A climbing image nudged elastic band method for finding saddle points and minimum energy paths. *J. Chem. Phys.* **113**, 9901–9904 (2000).

ACKNOWLEDGEMENTS

The research reported in this publication was supported by funding from King Abdullah University of Science and Technology (KAUST).

AUTHOR CONTRIBUTIONS

J.J. performed the calculations. All authors contributed to the data analysis and manuscript writing.

COMPETING INTERESTS

The authors declare no competing interests.

ADDITIONAL INFORMATION

Correspondence and requests for materials should be addressed to Udo Schwingenschlögl.

Reprints and permission information is available at http://www.nature.com/reprints

Publisher's note Springer Nature remains neutral with regard to jurisdictional claims in published maps and institutional affiliations.